Experimental Thermal and Fluid Science 149 (2023) 110998

Contents lists available at ScienceDirect

Experimental Thermal and Fluid Science

journal homepage: www.elsevier.com/locate/etfs

Extended-resolution of a single-camera synthetic Schlieren method for measurement of free liquid surfaces☆

Huixin Li [a], Duo Xu [a,b,*]

[a] The State Key Laboratory of Nonlinear Mechanics, Institute of Mechanics, Chinese Academy of Sciences, Beijing, 100190, China
[b] School of Engineering Science, University of Chinese Academy of Sciences, Beijing, 100049, China

ARTICLE INFO

Keywords:
Surface topography
Height of free surface
Synthetic Schlieren
Single camera

ABSTRACT

In a synthetic Schlieren method of measuring the height of a dynamic free liquid surface, the smallest wavelength of the measured surface topography is determined by the spatial resolution of the displacement field of markers. Currently, a displacement vector is obtained for each interrogation window, including a few markers, with a cross-correlation algorithm. In this study, the measurement resolution is extended by obtaining the displacement of individual markers. This simple and rational change, however, brings technical difficulties in numerically solving the governing equation over spatially randomly distributed markers. For this, the governing equation, which associates the surface height to be measured with the virtual displacements of the markers, is solved by the finite-volume scheme for the unstructured meshes, where a marker locates at the center of each triangular mesh face. The present method is examined with the synthetic generated data, in laboratory experiments of a transparent solid carved with a sinusoidal surface, and in experiments of water ripples. The measurement uncertainty is discussed.

1. Introduction

Liquid free surface widely exists in nature (e.g. ocean, rivers and lakes) and in engineering applications. For example, in coastal engineering, the free ocean surface waves generated by winds give non-trivial impacts on offshore platforms [1]. In aerospace devices, the liquid sloshing with substantial free surface motions is essential to the vibrations of propellant tank [2]. To get physical insights of such flows, the dynamics of the free surface are investigated in laboratory experiments, where the flow conditions are better controlled [e.g.3,4]. In the laboratory experiments, imaging techniques have advantages to give quantitative measurements of the free surface height and the surface topography, due to their high precision and non-intrusive nature (see a recent review of Gomit et al. [5] and references therein). These imaging techniques are usually based on the principle of light reflection [6,7] and refraction in particular [8–23].

In a pioneer study of Kurata et al. [8], a striped grating was placed below a shallow water channel, and a camera was positioned above the free (water) surface to capture the images of the grating. A reference image was captured when the free surface was still, and a refracted image was recorded when the surface ripples emerged. Comparing the reference and refracted images shows that the imaged grating was virtually displaced due to the light refraction at the free surface. They derived a relation of the surface topography with the virtual displacements of the grating, based on the Snell's law. In their method, a point where the surface height is nearly unchanged in time is needed as the reference height to reconstruct the two-dimensional surface height.

Following the same physical working principle of Kurata et al. [8], Tanaka et al. [10] and Moisy et al. [15] further developed this imaging method with replacing the grating with a pattern of spatially random markers. The latter, termed as free-surface synthetic Schlieren (FS-SS), had great care on technical details and on quantifying and analysis of the measurement errors. Their method presents an accurate and low-cost measurement of the topographic structures of the free surface, established with a single camera. In their method, random dots are printed on a transparent sheet, and the virtual displacements of these dots are quantified by the well-developed cross-correlation algorithm of particle image velocimetry (PIV). The displacement field is used to calculate the surface spatial gradients. Then the surface height is reconstructed using a least-square integration of the surface gradient with the spatially averaged surface height as the reference. Kolaas et al. [21] further developed the FS-SS method through illuminating the dot pattern with two light sources with different wavelengths (i.e. one visible blue and the other one near infrared), and the difference in refraction between the two-color patterns allows the evaluation of the surface gradient. Recently, Li et al. [24] extended the FS-SS method that

☆ This document is the results of the research project funded by the National Natural Science Foundation of China.
* Corresponding author at: The State Key Laboratory of Nonlinear Mechanics, Institute of Mechanics, Chinese Academy of Sciences, Beijing, 100190, China.
E-mail address: duo.xu@imech.ac.cn (D. Xu).

https://doi.org/10.1016/j.expthermflusci.2023.110998
Received 10 April 2023; Received in revised form 15 June 2023; Accepted 4 July 2023
Available online 8 July 2023

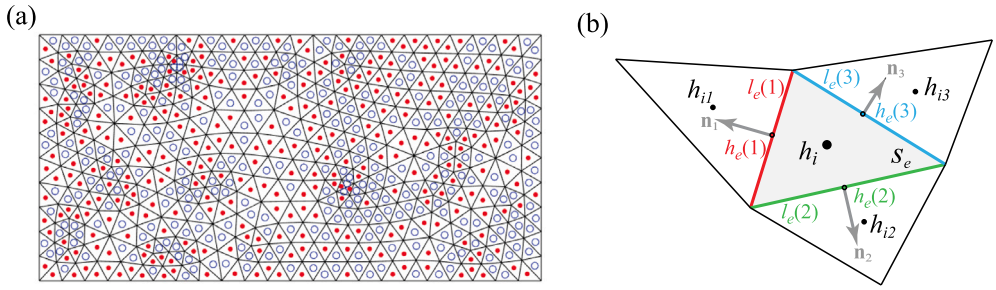

Fig. 1. (a) Schematic of the markers and the unstructured mesh. The red filled circles indicate the small diameter markers and the blue hollow circles denote the larger diameter markers. (b) A sketch illustration of finite-volume scheme for solving the governing equation. A black dot marks the geometric center of the element, and $\vec{n}$ indicates the normal direction of the edge.

no reference surface height is required to reconstruct the surface height, also using a single camera. This is advantaged that their measured wavelength of the surface topography can be as large as infinity in principle (flat free surface with height change). Their method uses the PIV cross-correlation algorithm to obtain the displacement field over evenly distributed grids, the same as Moisy et al. [15] and many others.

For obtaining the displacement field in the synthetic Schlieren method of e.g. [15,24], a refracted image is divided into small areas (interrogation windows) that several dot markers (8 to 10 dots in an optimized PIV configuration) are included in each window. The cross-correlation algorithm is used to obtain a displacement vector for each interrogation window that the vector represents the most probable motion of the dots in this window [25]. The size of the interrogation window determines the smallest wavelength of the measured surface wave. This featured wavelength is essential to retrieve the characteristics of turbulence below the surface or the characteristics of wind above the surface, which leaves the footprint (i.e. topographic structures) on the free surface [26,27].

In a recent experimental study, Mandel et al. [28] measured the free surface turbulence above a model of a vegetative canopy, which is composed of vertically mounted rigid cylinders. The authors took the rigid cylinders as the reference pattern (see their Fig. 3) and applied the method of Moisy et al. [15] to estimate the surface gradient. In this type of experiment and analogies, the reference pattern is difficult to become as spatially dense as the manufactured random dot pattern. As a result, the measurement resolution of the synthetic Schlieren method is limited under such conditions. One option for lowering the requirements on the number of reference markers in this situation is to track virtual displacement for individual markers rather than a bundle of them, following the concept of particle tracking velocimetry (PTV). The dot tracking algorithm itself has attracted much attention [29–33]. While in the synthetic Schlieren method, shapes, sizes and density of markers can be controlled in preparation of the marker sheet to help improving tracking individual markers, and importantly the virtual motions of these markers are within the plane (instead of miss-matching particles due to out-of-plane motion in two-dimensional PIV). Consequently, the displacements of the markers can be mostly captured. Recently, Rajendran et al. [34] proposed a dot tracking methodology for processing background-oriented Schlieren (BOS) images. Charruault et al. [35] developed a dot tracking methodology that allows tracking much stronger image deformations. Both dot tracking algorithms and others can be implemented to measure shorter surface wavelengths with the FS-SS method in principle. In practice, the displacement field of the randomly distributed markers requires proper interpolation to obtain the displacement field over evenly spaced grids (structured mesh), for using the finite-difference scheme in FS-SS [15] or in [24]. It is however challenging to justify the choice of the interpolation methods. An alternative route, avoiding the interpolation, is to implement the finite-volume scheme for the FS-SS method or similar.

In this study, the finite-volume-scheme form of the method of Li et al. [24] is introduced, while a hybrid PIV-PTV algorithm is used to obtain the displacements of individual dot markers. This simple change is found to help extending the resolution of the surface measurements. In an idealized condition of the marker configuration (in terms of their size and spatial distance and etc.), the present method assists to reveal possible smaller scale topographic structures. When the number of the markers is sometimes limited, as exampled above in [28], the present method looses the requirement on the amount of markers for reasonably capturing the surface topography, comparing with the methods [e.g.15,24] that the PIV cross-correlation is required with the finite-difference scheme.

The rest of the manuscript is structured as below. In Section 2, the detailed method is introduced. The examination of the method for the synthetic data is given in Section 3, while the experimental examination is presented in Section 4. A detailed discussion and conclusions are given in Sections 5 and 6, respectively.

2. Methodology

The present method shares the same governing equation with that of Li et al. [24], which is briefly presented below for completeness of the manuscript. According to the Snell's law, the equation governing the displacement $\boldsymbol{u}$ of markers and the surface height $h(x, y)$ is

$$\boldsymbol{u} = h\left[\tan\left(\tan^{-1}(\nabla h) + \sin^{-1}[r_n \cdot \sin(\boldsymbol{\alpha} - \tan^{-1}(\nabla h))]\right) - \tan(\boldsymbol{\alpha})\right],$$

where h is the surface height to be measured, $r_n = n_a/n_l$ the refractive index ratio between air and transparent material (e.g., water), and ∇ is the spatial gradient operator. $\boldsymbol{\alpha} = \alpha_x(x, y)\hat{x} + \alpha_y(x, y)\hat{y}$ quantifies the angle of the camera viewing the marker, where $\hat{x}$ and $\hat{y}$ are unit vectors along the x and y direction, respectively. $\boldsymbol{\alpha}$ can be obtained from a calibration procedure. This equation can be simplified by assuming that $\boldsymbol{\alpha}$ and ∇h are small (i.e., $\tan(\boldsymbol{\alpha}) \approx \boldsymbol{\alpha}$ and $\tan(\nabla h) \approx \nabla h$) as

$$\boldsymbol{u} = h \cdot (1 - r_n)(\nabla h - \boldsymbol{\alpha}). \tag{1}$$

Here $h(x, y)$ is the unknown to be determined.

The displacement $\boldsymbol{u}(x, y)$ can be obtained by the hybrid PIV-PTV algorithm to obtain the displacement of each individual marker. The sketch of the marker pattern is shown in Fig. 1(a). Two sizes of markers are used, and the diameter of one is about twice of that of another one, as demonstrated with the red filled and blue hollow circles, respectively. The two sizes of the markers help self-examining if the displacement of the marker is obtained correctly. For the spatially densely distributed markers, after the transformation of the refraction image based on the PIV displacement fields, a comparison of the transformed refracted image and the reference image shows that locally a marker in the refracted image is partially overlapped with multiple markers in the referred image. Comparing the size of the marker with the candidate markers helps better pairing the markers, so as the displacement, when necessary for a post-processing.

The triangulated meshes are generated to construct an unstructured mesh field, and Eq. (1) is solved by the finite volume method. The Eq. (1) is integrated over each mesh element,

$$\frac{1}{s_e}\int_s \boldsymbol{u}\,\mathrm{d}s = \frac{1}{s_e}\left(\frac{1-r_n}{2}\right)\int_s \nabla h^2\,\mathrm{d}s - \frac{1}{s_e}(1-r_n)\int_s \boldsymbol{\alpha} h\,\mathrm{d}s, \tag{2}$$

where $\int_s$ indicates the spatial integration operation over the element, and s_e is the area of the element. According to the Gauss's theorem, the first term on the right-hand side of the equation can be replaced by the line integration, $\int_s \nabla h^2 \mathrm{d}s = \int_l h^2 \mathbf{n}_l \mathrm{d}l$. For illustration, a sketch is shown in Fig. 1(b). For a target element i, the height is h_i, and $\int_s \nabla h_i^2 \mathrm{d}s \approx \nabla h_i^2 s_e \approx \sum_{i=1}^{3} h_e^2(i)\cdot l_e(i)\cdot \mathbf{n}_i$ in a discrete form, where h_e, l_e and $\mathbf{n}_i$ are the height at the edge of a triangular element, the length of the corresponding edge and the normal vector of the corresponding edge, respectively (see Fig. 1b). The unknown h_e^2 needs to be reconstructed by $h(x,y)$ at the center of neighboring elements. See numerical details on finite volume method in [36,37].

In Eqs. (1) and (2), $\boldsymbol{\alpha}$ needs to be obtained in a calibration procedure. The reference dot pattern is placed on the bottom of the setup, usually a transparent tank. A reference image is recorded when there is no liquid in the setup. Then the setup is filled with the transparent liquid and a refraction image is recorded when the liquid remains still. The height of the still surface is measured, so that ∇h is known. In the experiments presented in this study, the bottom of the setup is leveled and $\nabla h = 0$, so that $\boldsymbol{\alpha} = -\boldsymbol{u}_c/h_c/(1-r_n)$, where h_c is the height measured by a caliper and the displacement $\boldsymbol{u}_c$ is obtained through the hybrid PIV-PTV method for the paired reference and refraction images.

The displacements $\boldsymbol{u} = (u_x, u_y)$ are obtained on N mesh grid points, and at each point there is one h. For each direction, N equations are constructed with the corresponding component of the displacements, according to the discrete equation (1). Consequently, a linear system is constructed to contain $2N$ equations, which have N unknowns (i.e. h). This leads to an over-determined linear system. At the border of the computation domain, the reconstruction of the height at the border edge requires the element outside of the domain, so that the Neumann condition is used (by assuming that the spatial gradient of the height at the border is zero). In this study, the linear equation system was solved using the Matlab intrinsic function *fsolve* with the Levenberg–Marquardt algorithm. This is easy to implement for demonstrating the method. It is eventually an optimization process started with an initial guess. After $h(x,y)$ is solved, the coordinates of $h(x,y)$ need to be remapped, $(x,y)^* = (x,y) - h(x,y)\tan[\boldsymbol{\alpha}(x,y)]$, as mentioned in [15].

The routine of solving the governing equation is summarized in the following. The calibration procedure is firstly carried out to obtain $\boldsymbol{\alpha}$. Then the initial guess is prepared for nonlinear optimization in *fsolve*. Given that the hybrid PIV-PTV method is used to obtain the displacement field, the intermediate displacement field of the PIV step is applied to get a solution using the method of Li et al. [24]. Then this solution at the unstructured mesh grids is obtained by the linear interpolation, and is taken as the initial guess for the present method. Finally, the nonlinear optimization process via $fsolve$ is carried out to reach a converged solution. This routine gives converged solution in a few steps with the Matlab solver. The constant heights taken as the initial guess are also examined, and they can give a converged solution. However, these initial guesses cannot deviate from the solution too much, otherwise a wrong solution is reached because the nonlinear optimization gives local optimization.

3. Simulation examination

To quantify the performance of the present method, it is firstly examined using simulation data with an analytical solution. The simulated data were generated taking the form of surface height $h(x,y) = \sin[x/20 + (y+50)/40] + 10$, as shown in Fig. 2(a).

For the simulation examination, the angle $\boldsymbol{\alpha}$ is obtained through that a camera is assumed to be placed a certain distance from the marker pattern. Then the straight line connecting a marker and the camera and the camera optical axis establish an angle $\boldsymbol{\alpha}$ for each individual marker. The resulted $\boldsymbol{\alpha}$ is shown in Fig. 2(b) where a concentric circular distribution is seen. In addition, we need to obtain the displacements of markers for this analytical surface height. For this, the analytical surface height h and its analytical spatial gradient ∇h are obtained at the maker positions, and they are inserted into Eq. (1) together with $\boldsymbol{\alpha}$ to obtain the marker displacements $\boldsymbol{u}$. Finally, $\boldsymbol{u}$ is used to solve for $h(x,y)$ by the method introduced in Section 2.

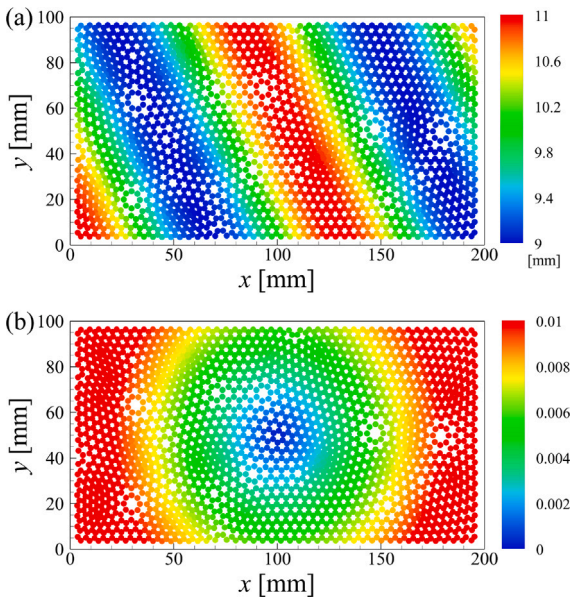

Fig. 2. (a) The contour map of the ground truth of the surface height of the simulated data. Each dot corresponds to a marker position. (b) The contour map of the angle $\boldsymbol{\alpha}$.

The present method was carried out with initial guesses of constant values. The solution is shown in Fig. 3(a), which visually agrees with the ground truth of the simulated data in Fig. 2(a). The effect of the initial guesses on the solution is examined, and the corresponding measurement absolute errors are shown in Fig. 3. The noticeable large absolute errors are seen over the area, presenting local fluctuations over the locally densely distributed markers. This might be caused by the elementary reconstruction scheme in the finite volume method used in this study. During the optimization process of solving the governing equation, the local numerical oscillation is not suppressed. This issue is expected to be possibly taken care of through advanced numerical scheme of finite volume method and/or the numerical method solving the over-determined linear system of the governing equations. For the same simulated surface height, the effect of the mesh grid number (number of markers) on the solution is examined. When the mesh grid number is increased from 648 to 2592, 10 368 and 41 472, the spatially averaged measurement absolute error of the surface height decreases from 0.06 to 0.04, 0.03 and 0.02, respectively, see Fig. 4. Correspondingly, the time for the computation substantially increases with the increase of the number of grids using *fsolve*. The time for the present method is expected to be largely reduced with an in-house solver, according to Li et al. [24]. For the practical experiments, the number of the markers is controlled when the marker template is prepared, and it needs to be adjusted according to the dimensions of the measurement area, the resolution of the camera sensor (a marker in the image takes 3 pixels at least in diameter), the scale range of the surface and other factors.

4. Experiments

Two experiments were carried out to demonstrate and examine the present method. One is a transparent solid that a sinusoidal wave is on

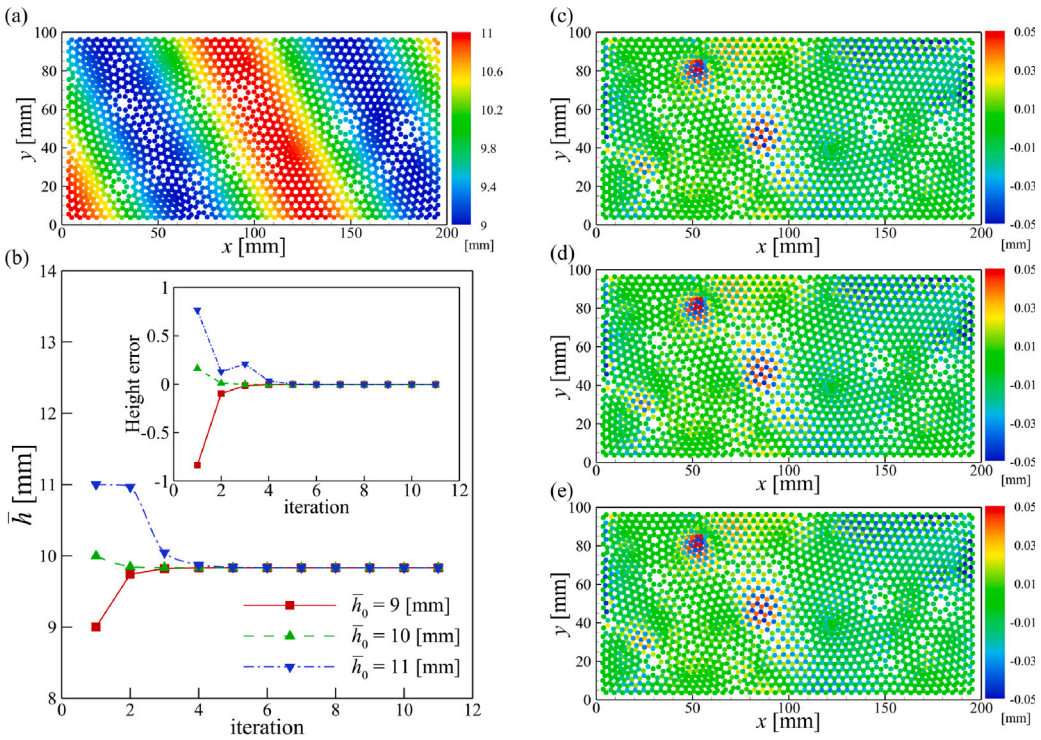

Fig. 3. (a) The contour map of the solved surface height with the simulated data (where the initial guess is 10). (b) The mean of the solved h and the absolute error of the solved height against iterations. (c–e) The contour map of the absolute error of the height with the initial guess of 11, 10 and 9, respectively.

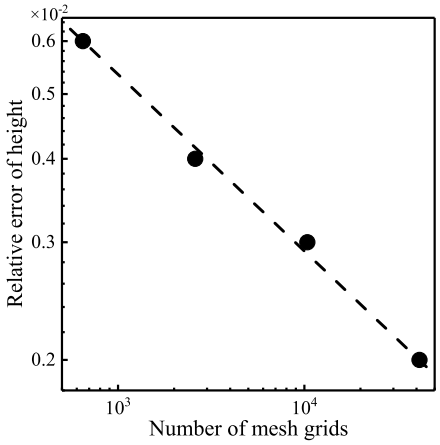

Fig. 4. The relative error of the surface height against the number of the mesh grid points from the simulation examination, where the dot line indicates a power fit of data with an exponent of about −1/4.

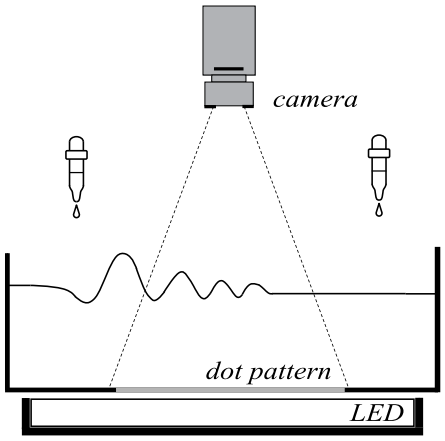

Fig. 5. The sketch of the experimental setup of the ripple surface caused by droplets.

one side while a flat surface is on the other side. The other experiment is to measure a ripple surface, which is obtained by releasing a droplet falling onto a still water layer. The two experiments were carried out with the same pattern and camera configuration.

4.1. Setup and measurement arrangement

A tank was manufactured with transparent acrylic plates, and it has dimensions of 200×200×200 mm^3 (length × width × height). The image of a random dot pattern was printed on an A4 transparent sheet and cut to be 100×50 mm^2, and it was attached upon the inner flat bottom of the tank, as sketched in Fig. 5. A white LED light (made of an array of small LED elements) was used to provide approximately uniform illumination for the marker pattern about 50 mm below the tank. A compact Basler camera (equipped with a lens of focal length 75 mm) was used. The brightness of the LED was adjusted so that the edge of the black dot markers can be clearly seen in the recorded images.

When the bottom of the empty tank was adjusted to be leveled, an image of the dot pattern was captured as the reference image (see Fig. 6a). When the water surface was still after being slowly filled into the tank, an image of the dot pattern was recorded, while the height of the surface is 10 ± 0.1 mm measured multiple times by a caliper. These two images were used to obtain the calibrated angle $\boldsymbol{\alpha}$ for each point (geometric center of the marker), as shown in Fig. 6(b), where the displacements of individual dots are color-rendered with the magnitudes of the displacements.

A sinusoidal surface wave with a wavelength of 18 mm and amplitude of 1 mm on the top surface of a 10 mm thick solid plate (material: Somos® WaterShed XC 11122, refractive index 1.514) was established

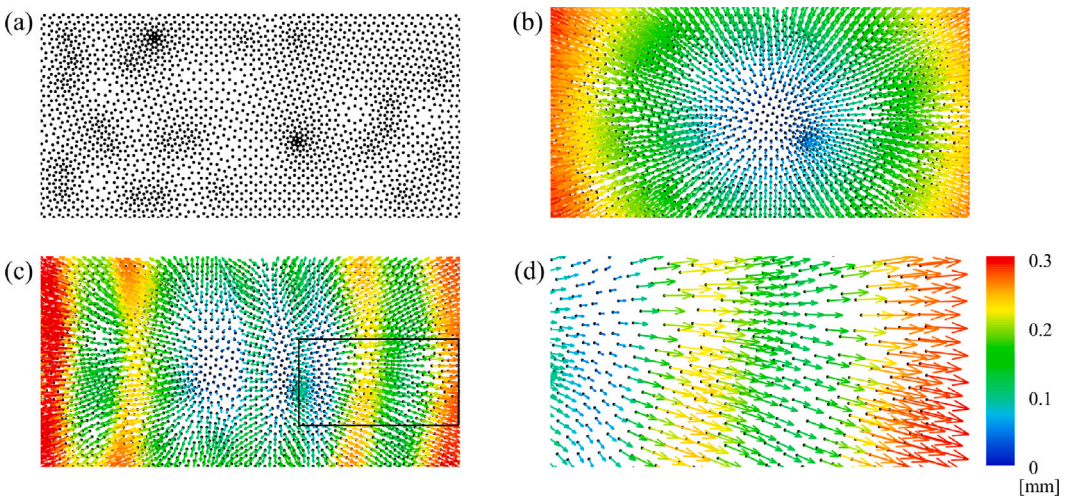

Fig. 6. (a) The raw image of the printed dot pattern. (b) The displacements of individual dots α in the calibration. (c) The displacements of the individual dots for a temporal sample of the ripples caused by a droplet. (d) The close-up of the displacements of the individual dots enclosed by a rectangular in (c). In (b–d), the displacements are color-coded with the magnitude of the displacements, and they share the same color legend.

by the three-dimensional (3D) printing technique. The size of the plate is 50×100 mm^2. The 3D printed plate was positioned on the top of a dot pattern. The camera was located about 700 mm above the dot pattern.

For the experiment of surface ripples, at beginning, a droplet (in diameter of about 4 mm) from a pipette (with inner diameter of 2 mm) locating close to one side of the tank (see Fig. 5) was released about 150 mm above the still water surface to generate the surface ripples. Following that, a droplet in similar size was released to fall onto the water layer (see Fig. 5) to generate a second group of ripples moving in the opposite direction. The sampling frequency is about 20 Hz. Other configurations of the experimental setup are the same as those used in the experiments of the solid with the sinusoidal surface. The images of the dot pattern were recorded and a temporal sample of the dot displacements (in reference of the image without water) is shown in Fig. 6(c–d). For the present configuration, the sizes of the dots in images are from about 7 pixels to 14 pixels. In the solid sinusoidal plane surface experiment, the maximum displacement of the dot pattern is about 16 pixels, while in the ripple surface experiment, it approximates 3.5 pixels. The hybrid PIV-PTV algorithm in Lavision Davis is used to compute the PIV-PTV displacement field with a multi-step algorithm (the interrogation window 96 × 96 pixel^2 for the first step and 48 × 48 pixel^2 for the last step). Subsequently, the displacement of each individual dot is determined using the PTV algorithm. The position of each dot is identified based on its highest intensity peak, and the exact shift of each dot is obtained by performing individual dot correlations between the reference and refracted images [38]. To examine the accuracy of the displacement vectors obtained using this hybrid PIV-PTV method, the dots in the refracted image are transformed back using these displacement vectors and compared with the dots in the reference image. (The comparison of the dots in the two images may serve as an indicator of the measurement accuracy of the displacement vectors.)

4.2. Results

The 3D modeling and real picture of the acrylic-like plate are shown in Fig. 7(a) and (b). The reconstructed topography (c) by the present method and corresponding topography (d) by the method with the finite-difference scheme of Li et al. [24] are compared with the ground truth. The reconstructed topography from (c) is projected onto the same mesh grids as those used in Fig. 7(d). The profiles of both results are then averaged along the y direction, respectively, where the standard deviation of the profiles along the y direction is taken as the error bar. The two profiles, together with the ground truth, are shown in Fig. 7(e). The height of the 3D printed object was measured by a caliper for 5 times at crests and troughs of the wave, and the respective standard deviations (±0.05 mm) are used as the error bars shown in Fig. 7(e). The wavelength measured from the present reconstructed profile is 18 ± 0.3 mm, which slightly over-estimates the ground truth about 1.7%. For the reconstructed heights, the topography of the present method agrees well with that from the raw model. The spatial average deviation between the result of the present method and the ground truth (with the uncertainty) is 0.03 mm, approximately 0.3% in relative error with the corresponding height in the ground truth, while the maximum relative error of the measured height is about 2%.

Three snapshots of the surface ripples measured by the present method are shown in Fig. 8(a, c, e). In Fig. 8(a), the topography of the ripples is temporally close to the initial formation of the ripples, where the larger oscillation of the surface height can be seen, and as farther away from this point the oscillation amplitude of the surface height gradually decreases. About 4 seconds after Fig. 8(a), a similar sized droplet fell on the water surface, and the surface topography in Fig. 8(c) shows approximate symmetry to that from Fig. 8(a). After some seconds, the distinct ripples produced by both droplets moved out of the field-of-view, and the surface topography turns to Fig. 8(e). The FS-SS method of Moisy et al. [15] is well applicable for the ripple experiments, and it was used for the same images for comparison. The respective results at the same times are shown in Fig. 8(b, d, f). These results are visually in good agreement with those in Fig. 8(a, c, e). The spatial average difference of the results between the present method and the FS-SS method is about 0.02 mm, after projecting the results in Fig. 8(b, d, f) onto the coordinates of the dots in Fig. 8(a, c, e). The very small difference (about 0.2%) demonstrates that the present method is applicable for this case. This is established given that the density of the dot pattern supports resolving the wavelength of the ripples. When this condition is not satisfied, the measurement errors increase, see discussion in [15,24] on the finite-difference scheme, as well as the discussion on the comparison between the finite-difference and the finite-volume scheme in Section 5 of this study.

5. Discussion

The present method shares the same working principle as Li et al. [24] and takes a close analogy to Moisy et al. [15], hence the measurement uncertainty and the breakdown condition of the working principle are the same as these two methods.

The main difference between the present method to that of Li et al. [24] is on the boundary condition that the latter does not necessarily

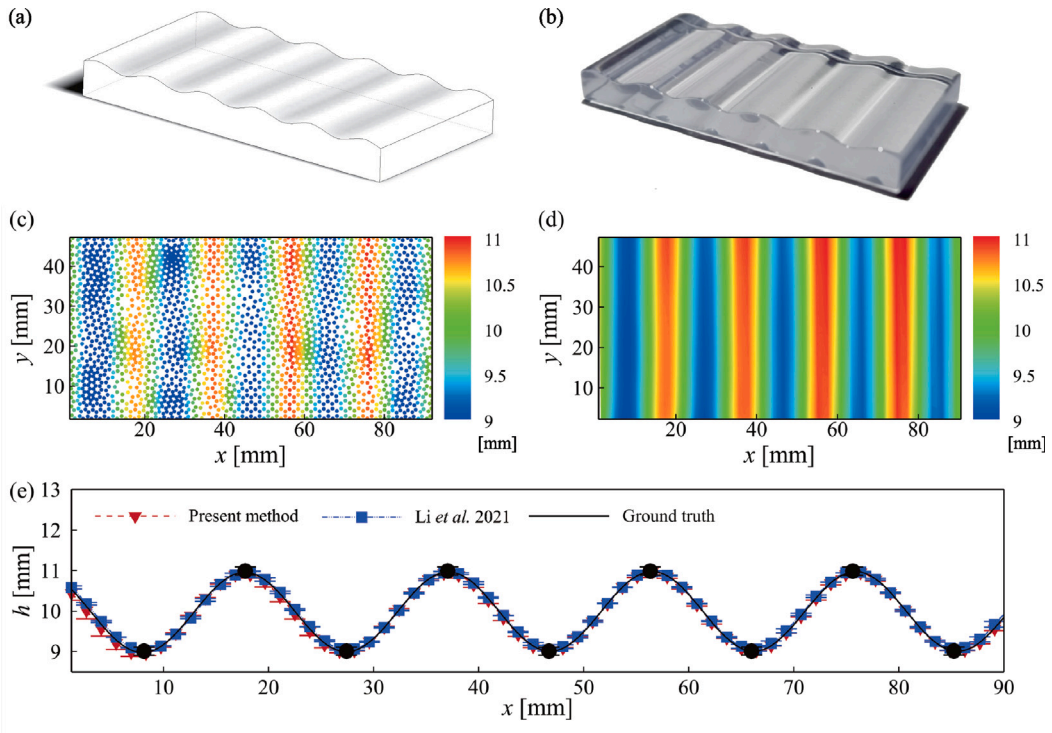

Fig. 7. (a) The rendering image of 3D model of the transparent solid with a sinusoidal surface. (b) The real picture of the 3D printed object. The result of the surface topography measured by the present method (c) and the method of Li et al. [24] (d), as well as the profiles averaged along the y direction respectively (e). The error bars indicate the standard deviation of the height along the y direction.

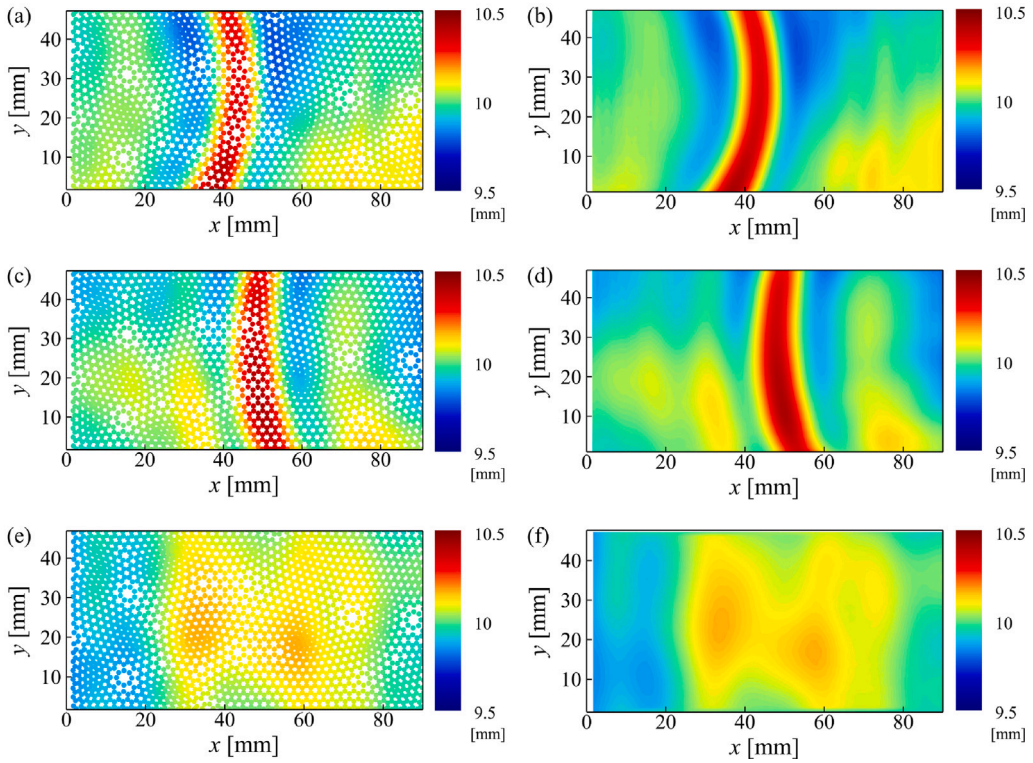

Fig. 8. The snapshots of the topography structures of the water ripples from the present method (a, c, e) and the FS-SS method (b, d, f).

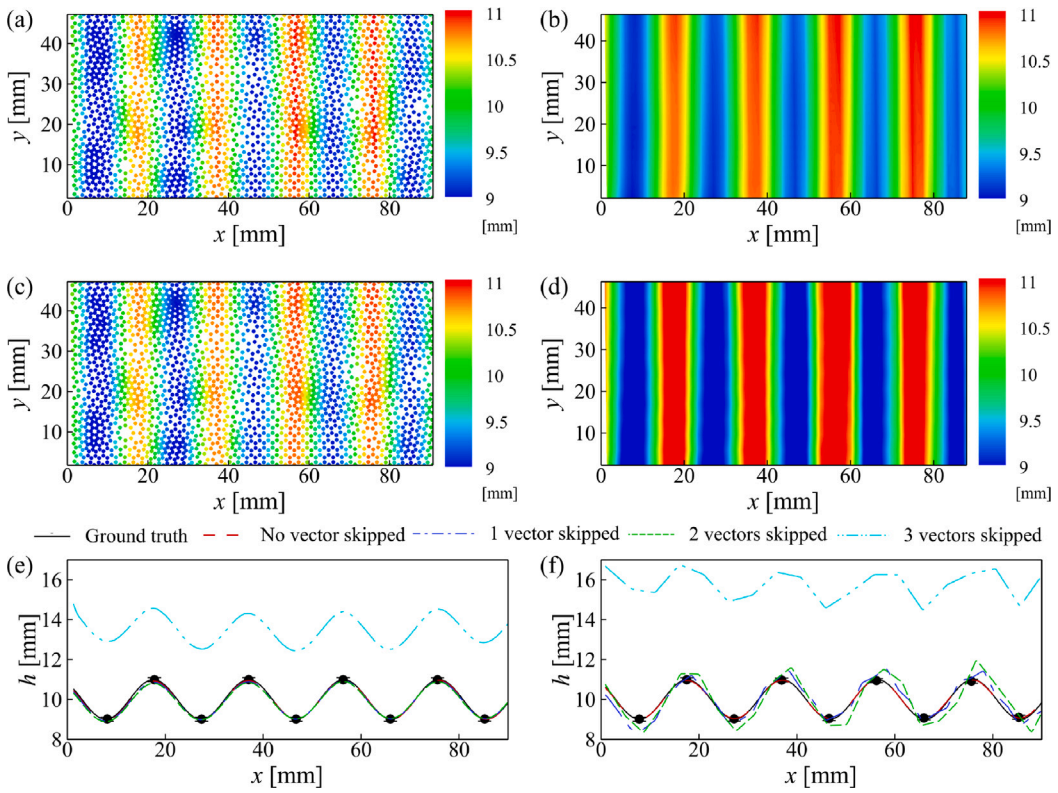

Fig. 9. The measurement results of the 3D printed plate from the present method (a, c, e) and the finite-difference scheme over the structured mesh grids (b, d, f). One vector is skipped over the structured mesh grids along each direction to get the result in (b), and two vectors skipped for (d). The results in (b) and (d) are taken as the initial guess for (a) and (c), respectively.

need the implementation of the boundary condition. Due to the reconstruction in the finite volume method, the boundary condition is necessary for the present method, and the Neumann condition is used here. With the Neumann condition, when the initial guess (either a constant value or a solution from [24]) is not far from the solution, the Matlab solver can give a converged and correct solution.

The method here is sensitive to camera vibration, provided that the vibration gives direct influence to the displacement field in both the experimental measurement and the calibration (according to Eq. (1)). To limit the camera vibration encountered in the cooling fan of the high-speed camera, a compact low-sampling rate camera (free of a cooling fan) was used. The vibration of the camera, optical table and aluminum profile framework for the setup produced approximately 0.05 pixel displacements in images of a still target. When a high-speed camera with a cooling fan is used, particular care is required in mounting the camera to improve its stability. The influence of the camera vibration on the measured surface is examined and can be referred in [15,24] and not repeated here.

According to Eq. (2), the measurement uncertainties of the surface height are found to be from three sources, the virtual displacement $\boldsymbol{u}$, $\boldsymbol{\alpha}$ and the refractive indices n_a and n_l. The main source of uncertainty is from that of measured displacement. In this study, the displacement from the PIV cross-correlation is essential to the displacement for individual markers, given that the local matching of the marker position relies on the initial transformation of the reference image which is obtained from the PIV cross-correlation operation. The displacement field of dots was obtained in Lavision Davis, and the uncertainty is expected to be around 0.1 pixel, estimated from subtracting the transformed image according to the displacement from the reference image. Given the nonlinearity of Eq. (1), the uncertainty propagation in the linear system is infeasible here. For a similar problem in background-oriented Schlieren technique, Rajendran et al. [39] used sparse linear operators in a Poisson solver for estimating the measurements uncertainty. We found the present nonlinear equation (2) is difficult to be adapted in the such way. Thus, a Monte-Carlo-simulation style method for uncertainty estimation is applied [40,41], and random noise was added to two components of displacement fields. The noise is Gaussian distribution with a mean of 0.1 pixel and a standard deviation of 0.05 pixel. The signs of the values were randomly chosen. Then the contaminated displacement field was used to calculate the surface height again. This procedure was repeated 100 times and for each time the noise was randomly generated. The uncertainty of the calibration angle can be obtained from uncertainty propagation, and the uncertainty of displacement 0.1 pixel, the uncertainty of the surface height in the calibration 0.1 mm and the uncertainty of the refractive index 5×10^{-5} are considered here. The analysis was implemented on the data synthetically generated (as shown in Fig. 3a). The relative uncertainty of the measured height is approximately 0.2% in average and a standard deviation of 1.2%.

The spatial resolution of the displacement $\boldsymbol{u}$ is essential to the measurements of the surface topography (i.e. the smallest wavelength). We consider the case shown in Fig. 7 for the test. The dots in the pattern are dense for the surface wave that both the present method and that with the finite-difference scheme give nearly the same results, see Fig. 7. Then the vectors at the structured mesh grids (from the PIV correlation) are sub-sampled with one, two and three neighboring vectors skipped from each direction. With more vectors skipped, the resolution of the vectors for the finite-difference scheme gets farther away for resolving the surface wave (dissatisfying the Nyquist condition), and the respective results of the finite-difference scheme get worse (see Fig. 9b, d, f). Eventually, finer spatial resolution among the markers is not taken advantaged in this type of methods. However, when these results are used as the initial guess for the present method (after the interpolation), the embedded finer spatial resolution among the markers is employed to get better results, see Fig. 9(a, c, e). The number of dots used above is 2592, sufficient for resolving the target surface. Another test was conducted using the pattern of 162 dots

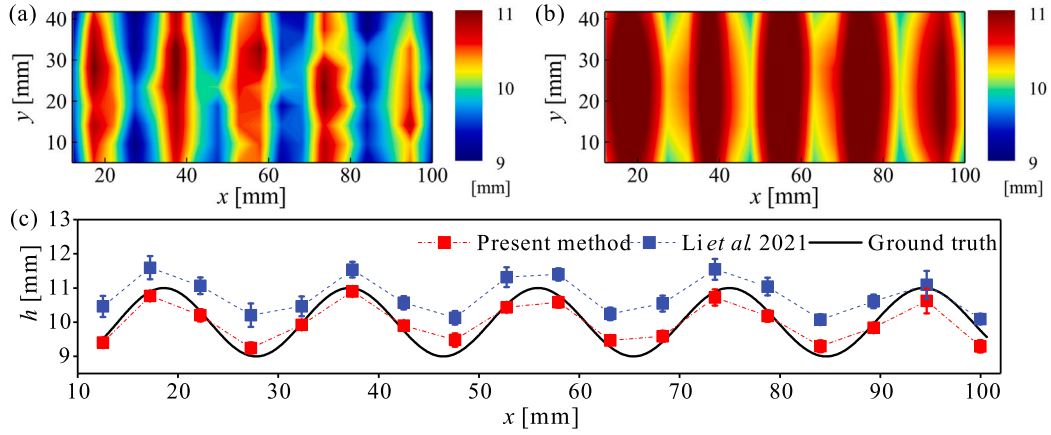

Fig. 10. The surface topography was measured using patterns with lower dot density. (a) The result obtained using the present method after being projected onto structured mesh grids. (b) The result obtained using the method of Li et al. [24]. (c) The profiles averaged along the y direction respectively for both methods, where the error bars indicate the standard deviation of the height along the y direction.

(approximately 4–5 dots per wavelength) to assess the performance of the proposed method with lower dot density. Fig. 10(a) presents the results obtained using the proposed method based on the PIV-PTV displacement field (after projecting the result over evenly spaced grids for making contours). Linear interpolation was carried out over the scattered markers to obtain the displacements on the evenly spaced grids, which is 18 (in the x direction) × 9 (in the y direction) = 162 (the same number of scatter markers in the pattern). Then the method of Li et al. [24] was employed, and the result is shown in Fig. 10(b). In Fig. 10(c), the mean profiles averaged along y direction respectively from both methods are compared with the ground truth. The average relative error is approximately 0.8% for the present method based on the finite-volume scheme and 6.9% for the method of Li et al. [24] based on the finite-difference scheme. The results demonstrate that the proposed method, utilizing finite-volume scheme, may give better measurement results for the condition that the Nyquist condition is marginally satisfied. These results suggests that the present method is expected to help the application of the synthetic Schlieren method in the experimental condition similar to environments of Mandel et al. [28].

6. Conclusion

In this paper, we introduce a method to extend the resolution of the synthetic Schlieren method for measuring the height of a dynamic free surface. In this method, the free surface height is associated with the displacement of each individual marker, and the displacement is obtained by the hybrid PIV-PTV algorithm. Differing to the previous methods with the finite-difference scheme over the structured mesh grids, in this study, the *finite-volume scheme* is applied to solve the integrated form of the governing equation over the randomly distributed grids. The reconstruction of the surface height at the geometric center of a triangular element requiring the height of the triangular edges needs imposing the Neumann boundary condition at the domain border. The conception of extending the resolution is implemented and demonstrated based on the method of Li et al. [24], and it is expected to also work for the method of Moisy et al. [15] or others.

This method is examined through the synthetic data with the ground truth available. The present method shows that it can measure the two-dimensional surface wave well, that the relative error is about one percent. Finer the mesh resolution, smaller the relative error. The method is also examined and demonstrated in two laboratory experiments. One is the 3D printed transparent solid with a sinusoidal surface. The measurement results of the present method agree with the manufactured surface. Another experiment is to measure the surface ripples generated by droplets. The results of the present method and those of Moisy et al. [15] agree well.

In sharing the same (and analogical) working principle as Moisy et al. [15] and Li et al. [24], the main contribution of the uncertainty is from that of the displacement of the markers. For the presented method, the measurement results are sensitive to vibrations, although a fan-free compact camera is used to avoid the camera vibration resulting from the cooling fan. This is because that the vibrations bring in the direct error change of marker displacement, which results in the measurement errors on the surface height according to the governing equation.

The present method helps revealing possible smaller scale topographic structures, when markers are densely distributed. If the number of the markers is limited, our method might still capture the characteristic surface topography, given that the present method may take the use of the marker-marker denser spatial resolution, which is embedded but overlooked in the methods using the PIV cross-correlation algorithm to obtain the displacement field over the structured mesh grids where the finite-difference scheme is applicable.

CRediT authorship contribution statement

Huixin Li: Investigation, Methodology, Writing – original draft, Writing – reviewing & editing. **Duo Xu:** Conceptualization, Methodology, Writing – original draft, Writing – reviewing & editing, Supervision.

Declaration of competing interest

The authors declare that they have no known competing financial interests or personal relationships that could have appeared to influence the work reported in this paper.

Data availability

Data will be made available on request.

Acknowledgments

This work was supported by National Natural Science Foundation of China (No. 11988102 and 92152106). The authors thank Prof. Baofang Song (Peking University, China), Dr. Lixing Zhu and Dr. Yi Liu (Institute of Mechanics, Chinese Academy of Sciences, China) for the discussion on the finite volume method, and the technician for technical support.

References

[1] L.H. Holthuijsen, Waves in Oceanic and Coastal Waters, Cambridge University Press, 2007.

[2] R. Ibrahim, Liquid Sloshing Dynamics: Theory and Applications, Cambridge University Press, 2005.

[3] A. Paquier, F. Moisy, M. Rabaud, Surface deformations and wave generation by wind blowing over a viscous liquid, Phys. Fluids 27 (12) (2015) 122103.

[4] A. Charogiannis, J.S. An, C.N. Markides, A simultaneous planar laser-induced fluorescence, particle image velocimetry and particle tracking velocimetry technique for the investigation of thin liquid-film flows, Exp. Therm Fluid Sci. 68 (2015) 516–536.

[5] G. Gomit, L. Chatellier, L. David, Free-surface flow measurements by non-intrusive methods: a survey, Exp. Fluids 63 (2022) 94.

[6] N.A. Vinnichenko, A.V. Pushtaev, Y.Y. Plaksina, A.V. Uvarov, Measurements of liquid surface relief with moon-glade background oriented Schlieren technique, Exp. Therm Fluid Sci. 114 (2020) 110051.

[7] H. Hu, B. Wang, K. Zhang, W. Lohry, S. Zhang, Quantification of transient behavior of wind-driven surface droplet/rivulet flows using a digital fringe projection technique, J. Vis. 18 (4) (2015) 705–718.

[8] J. Kurata, K.T.V. Grattan, H. Uchiyama, T. Tanaka, Water surface measurement in a shallow channel using the transmitted image of a grating, Rev. Sci. Instrum. 61 (2) (1990) 736–739.

[9] X. Zhang, C.S. Cox, Measuring the two-dimensional structure of a wavy water surface optically: A surface gradient detector, Exp. Fluids 17 (4) (1994) 225–237.

[10] G. Tanaka, K. Okamoto, H. Madarame, Experimental investigation on the interaction between polymer solution jet and free surface, Exp. Fluids 29 (2) (2000) 178–183.

[11] N.J.W. Morris, Image-Based Water Surface Reconstruction with Refractive Stereo, University of Toronto, 2004.

[12] B. Jähne, M. Schmidt, R. Rocholz, Combined optical slope/height measurements of short wind waves: principle and calibration, Meas. Sci. Technol. 16 (10) (2005) 1937.

[13] R. Savelsberg, A. Holten, W. van de Water, Measurement of the gradient field of a turbulent free surface, Exp. Fluids 41 (4) (2006) 629–640.

[14] A. Fouras, D.L. Jacono, G.J. Sheard, K. Hourigan, Measurement of instantaneous velocity and surface topography in the wake of a cylinder at low Reynolds number, J. Fluids Struct. 24 (8) (2008) 1271–1277.

[15] F. Moisy, M. Rabaud, K. Salsac, A synthetic Schlieren method for the measurement of the topography of a liquid interface, Exp. Fluids 46 (6) (2009) 1021.

[16] I. Ng, V. Kumar, G.J. Sheard, K. Hourigan, A. Fouras, Experimental study of simultaneous measurement of velocity and surface topography: in the wake of a circular cylinder at low Reynolds number, Exp. Fluids 50 (3) (2011) 587–595.

[17] G. Gomit, L. Chatellier, D. Calluaud, L. David, Free surface measurement by stereo-refraction, Exp. Fluids 54 (6) (2013) 1540.

[18] G. Gomit, G. Rousseaux, L. Chatellier, D. Calluaud, L. David, Spectral analysis of ship waves in deep water from accurate measurements of the free surface elevation by optical methods, Phys. Fluids 26 (12) (2014) 122101.

[19] F. Aureli, S. Dazzi, A. Maranzoni, P. Mignosa, A combined colour-infrared imaging technique for measuring water surface over non-horizontal bottom, Exp. Fluids 55 (3) (2014) 1701.

[20] L. Engelen, S. Creëlle, L. Schindfessel, T. De Mulder, Spatio-temporal image-based parametric water surface reconstruction: a novel methodology based on refraction, Meas. Sci. Technol. 29 (3) (2018) 035302.

[21] J. Kolaas, B.r.H. Riise, K. Sveen, A. Jensen, Bichromatic synthetic Schlieren applied to surface wave measurements, Exp. Fluids 59 (8) (2018) 128.

[22] A.S. González-Vera, T.J.S. Wilting, A.P.C. Holten, G.J.F. van Heijst, M. Duran-Matute, High-resolution single-camera photogrammetry: incorporation of refraction at a fluid interface, Exp. Fluids 61 (1) (2020) 1–19.

[23] A. Simonini, D. Fontanarosa, M.G. De Giorgi, M.R. Vetrano, Mode characterization and damping measurement of liquid sloshing in cylindrical containers by means of reference image topography, Exp. Therm Fluid Sci. 120 (2021) 110232.

[24] H. Li, M. Avila, D. Xu, A single-camera synthetic Schlieren method for the measurement of free liquid surfaces, Exp. Fluids 62 (2021) 227.

[25] M. Raffel, C.E. Willert, F. Scarano, C.J. Kähler, S.T. Wereley, J. Kompenhans, Particle image velocimetry: a practical guide, Springer, 2018.

[26] R. Savelsberg, W. van de Water, Turbulence of a free surface, Phys. Rev. Lett. 100 (3) (2008) 034501.

[27] X. Guo, L. Shen, Numerical study of the effect of surface waves on turbulence underneath. Part 1. Mean flow and turbulence vorticity, J. Fluid Mech. 733 (2013) 558–587.

[28] T.L. Mandel, I. Rosenzweig, H. Chung, N.T. Ouellette, J.R. Koseff, Characterizing free-surface expressions of flow instabilities by tracking submerged features, Exp. Fluids 58 (11) (2017) 1–14.

[29] A. Adamczyk, L. Rimai, 2-dimensional particle tracking velocimetry (PTV): technique and image processing algorithms, Exp. Fluids 6 (6) (1988) 373–380.

[30] A. Stitou, M. Riethmuller, Extension of PIV to super resolution using PTV, Meas. Sci. Technol. 12 (9) (2001) 1398.

[31] M.H. Qureshi, W.-H. Tien, Y.-J.P. Lin, Performance comparison of particle tracking velocimetry (PTV) and particle image velocimetry (PIV) with long-exposure particle streaks, Meas. Sci. Technol. 32 (2) (2020) 024008.

[32] N.D. Cardwell, P.P. Vlachos, K.A. Thole, A multi-parametric particle-pairing algorithm for particle tracking in single and multiphase flows, Meas. Sci. Technol. 22 (10) (2011) 105406.

[33] C. Cierpka, B. Lütke, C.J. Kähler, Higher order multi-frame particle tracking velocimetry, Exp. Fluids 54 (5) (2013) 1–12.

[34] L.K. Rajendran, S.P. Bane, P.P. Vlachos, Dot tracking methodology for background-oriented schlieren (BOS), Exp. Fluids 60 (11) (2019) 1–13.

[35] F. Charruault, A. Greidanus, W.-P. Breugem, J. Westerweel, A dot tracking algorithm to measure free surface deformations, in: Proceedings 18th International Symposium on Flow Visualization, ETH Zurich, 2018.

[36] J. Blazek, Computational Fluid Dynamics: Principles and Applications, Butterworth-Heinemann, 2015.

[37] F. Moukalled, L. Mangani, M. Darwish, The Finite Volume Method in Computational Fluid Dynamics, Springer Cham, 2016.

[38] R. Theunissen, A. Stitou, M. Riethmuller, A novel approach to improve the accuracy of PTV methods, in: 12th International Symposium on Applications of Laser Techniques To Fluid Mechanics, Lisbon, Portugal, 2004, pp. 12–15.

[39] L.K. Rajendran, S.P. Bane, P.P. Vlachos, Uncertainty amplification due to density/refractive index gradients in background-oriented schlieren experiments, Exp. Fluids 61 (6) (2020) 1–16.

[40] C.E. Papadopoulos, H. Yeung, Uncertainty estimation and Monte Carlo simulation method, Flow Meas. Instrum. 12 (4) (2001) 291–298.

[41] H.W. Coleman, W.G. Steele, Experimentation, Validation, and Uncertainty Analysis for Engineers, John Wiley & Sons, Hoboken, 2018.